A hidden jet emission component revealed by the anomalous X-ray low state of 1ES 0229+200*

Ze-Rui Wang (王泽睿)[1,7†] Rui Xue (薛瑞)[2‡] Dingrong Xiong (熊定荣)[3,4,5§] Yun-Bing Xu (徐云冰)[6]
Lei-Ming Du (杜雷鸣)[6] Zhao-Hua Xie (谢照华)[6]

[1]College of Physics and Electronic Engineering, Qilu Normal University, Jinan 250200, China
[2]Department of Physics, Zhejiang Normal University, Jinhua 321004, China
[3]Yunnan Observatories, Chinese Academy of Sciences, 396 Yangfangwang, Guandu District, Kunming, 650216, China
[4]Center for Astronomical Mega-Science, Chinese Academy of Sciences, 20A Datun Road, Chaoyang District, Beijing, 100012, China
[5]Key Laboratory for the Structure and Evolution of Celestial Objects, Chinese Academy of Sciences, 396 Yangfangwang, Guandu District, Kunming, 650216, China
[6]Department of Physics, Yunnan Normal University, Kunming 650500, China
[7]Shandong Key Laboratory of Space Environment and Exploration Technology, China

Abstract: In August 2021, simultaneous *Swift*-XRT and *NuSTAR* observations recorded the extreme high-synchrotron-peaked BL~Lac object 1ES~0229+200 in an exceptionally faint X-ray state. The spectrum was concave, showing tentative hardening above ~ 25 keV. We investigate three representative interpretations within a common decelerating-jet framework: a one-zone hybrid electron–proton synchrotron model (Model A), together with external-Compton (EC) and pure synchrotron self-Compton (SSC) realizations of a two-zone leptonic model (Model B). All three reproduce the simultaneous X-ray spectrum. In Model A, electron synchrotron emission accounts for the soft X-rays, while proton synchrotron emission produces the hard component. In both realizations of Model B, a compact inner zone produces the hard component through EC or SSC emission, while an outer zone approximately describes the historical broadband emission. The three solutions therefore lead to the same observational inference: the low state reveals an additional radiative component that is normally hidden beneath the dominant soft-X-ray continuum. The present data do not determine whether this component arises from a second particle population in one zone or from a distinct dissipation region. Simultaneous hard-X-ray, MeV, GeV, and VHE observations will distinguish these possibilities.

Keywords: BL Lacertae objects: individual (1ES 0229+200), galaxies: jets, radiation mechanisms: non-thermal

DOI: 10.1088/1674-1137/aec118 **CSTR:**

CPC Accepted

I. INTRODUCTION

1ES 0229+200 is one of the most extreme high-synchrotron-peaked BL Lac objects (EHBLs) known, at a redshift of $z = 0.1396$ [1]. It is characterized by an exceptionally hard very-high-energy (VHE) spectrum and negligible accretion-disk signatures, properties that have made it one of the most extensively studied EHBLs for constraining the extragalactic background light (EBL) and intergalactic magnetic fields (IGMF; e.g., [2−4]). Under standard assumptions, its broadband spectral energy distribution (SED) has generally been well described by one-zone synchrotron self-Compton (SSC) emission from a single population of relativistic electrons [5, 6].

In August 2021, Wierzcholska and Siejkowski [7] reported an anomalous X-ray low state based on simultaneous *Swift*-XRT and *NuSTAR* observations. The concave spectrum suggested hardening near 25 keV, although limited photon statistics above 30 keV leave the detailed spectral continuation uncertain. Wierzcholska and Siejkowski [7] briefly discussed both leptonic and hadronic interpretations of this feature. These interpretations provide the context for the representative radiation models considered here. The source was too faint to yield a

Received 10 August 2026; Accepted 12 November 2026

* This work is supported by the National Key R&D Program of China (2023YFB4503305); the National Natural Science Foundation of China under Grants No. 12263009, No. 12473020, No. 12473042, No. 12373109, No. 12203043, and No. 12203024; and the Yunnan Province Youth Top Talent Project (Grant No. YNWR-QNBJ-2020-116)

† E-mail: zerui_wang62@163.com
‡ E-mail: ruixue@zjnu.edu.cn
§ E-mail: xiongdingrong@ynao.ac.cn

©2027 Chinese Physical Society and the Institute of High Energy Physics of the Chinese Academy of Sciences and the Institute of Modern Physics of the Chinese Academy of Sciences and IOP Publishing Ltd. All rights, including for text and data mining, AI training, and similar technologies, are reserved.

useful simultaneous short-timescale *Fermi*-LAT spectrum. We therefore use the simultaneous *Swift*-XRT and *NuSTAR* points for the X-ray comparison and use archival GeV–TeV measurements only as non-simultaneous constraints against flux overproduction.

Degeneracy among different radiation-mechanism interpretations has long been recognized as a major challenge in blazar emission modeling, because both electron-dominated and proton-based scenarios can reproduce similar broadband spectral energy distributions while requiring substantially different particle populations, magnetic fields, and jet energetics [8−10]. This ambiguity is particularly relevant for extreme high-synchrotron-peaked BL Lac objects, where the extreme parameter requirements of one-zone leptonic models have motivated alternative hadronic interpretations [11, 12]. Recent observations of anomalous high-energy spectral features have further highlighted this degeneracy. For example, the hard VHE spectral feature around 20 TeV reported in M87 by LHAASO can be reproduced by multiple physically distinct scenarios involving different particle populations and emission regions [13]. A broader study of LHAASO-detected blazars similarly demonstrated that leptonic, hadronic, and structured-jet scenarios can reproduce comparable broadband spectra while implying substantially different jet powers [14]. These examples illustrate that broadband spectral features alone may not uniquely identify the dominant radiation mechanism, motivating joint consideration of spectral, energetic, and multiwavelength constraints.

In this paper, we examine two physically distinct interpretations of the 2021 X-ray low state of 1ES 0229+200: (A) a one-zone proton-synchrotron model with co-spatial electron synchrotron emission and (B) a two-zone purely leptonic model. For Model B, we test both an external Compton (EC) realization and a pure SSC realization; in each case, a compact inner region produces the hard X-ray component, while an outer region approximately reproduces the historical broadband emission. We describe the modeling approaches in Section II, compare their physical parameters and energetic requirements in Section III, and discuss their observational implications in Section IV without favoring either as the unique explanation. In this work, we adopt the following cosmological parameters: $H_0 = 68\,\mathrm{km\,s^{-1}\,Mpc^{-1}}$, $\Omega_\Lambda = 0.7$, and $\Omega_\mathrm{M} = 0.3$.

II. EMISSION SCENARIOS

To enable a direct comparison between the leptonic and hybrid leptohadronic interpretations, we adopt a unified jet parameterization framework for both scenarios. This approach allows the physical requirements of the two models to be evaluated within the same dynamical context, including their differences in magnetic field strength, bulk motion, and emission-region location. In particular, the values of (Γ_0, B_0) at the reference distance r_0 allow a direct comparison of the jet conditions required by a purely leptonic scenario and by a hybrid electron–proton synchrotron scenario. Following the decelerating-jet parameterization of Wang et al. [15], we let the bulk Lorentz factor Γ and the comoving magnetic field B decline with distance r from the central engine. We embed the emitting regions in a conical jet, whose geometry we specify separately below. Both quantities are calibrated at the reference distance $r_0 = 0.1$ pc and are parameterized as

$$\Gamma(r) = \Gamma_0 - \frac{\Gamma_0 - 2}{\ln(\frac{100\,\mathrm{pc}}{r_0})} \ln\left(\frac{r}{r_0}\right), \tag{1}$$

$$B(r) = B_0 \left(\frac{r_0}{r}\right). \tag{2}$$

This parameterization describes a jet that gradually decelerates and has a declining magnetic field, reaching $\Gamma = 2$ at $r = 100$ pc. The transverse radius of the jet cross-section at distance r is $R(r) = r\tan\theta_j$, which is adopted as the characteristic radius of the spherical emitting region. The corresponding Doppler factor is evaluated as

$$\delta(r) = \left[\Gamma(r)\left(1 - \cos\theta_j \sqrt{1 - \Gamma(r)^{-2}}\right)\right]^{-1}. \tag{3}$$

We assume a viewing angle equal to the jet half-opening angle, $\theta_\mathrm{obs} = \theta_j$. Each scenario below contains one or two discrete spherical emitting regions along this jet profile, and each region inherits its local Γ, B, R, and δ from its distance r. The two scenarios are therefore calibrated independently and adopt different jet parameters (Γ_0, B_0). The value $r_0 = 0.1$ pc is the common normalization point at which B_0 and Γ_0 are defined; changing it leaves the physical profile unchanged after renormalization. Neither the jet half-opening angle nor the viewing angle has been measured directly for 1ES 0229+200. We therefore fix $\theta_j = \theta_\mathrm{obs} = 1.8°$ as a simplifying geometrical assumption rather than a source-specific observational constraint. The corresponding full opening angle, 3.6°, lies within the observed range of intrinsic opening angles of parsec-scale AGN jets [16]. The emitting-region location r is adjusted. A conical jet with its apex at the black hole then gives $R = r\tan\theta_j$, while the local Γ, B, and δ follow from Eqs. (1)–(3). Thus each Model-B zone adds one location parameter rather than four independent parameters R, B, Γ, and δ. For Model A, the manually adjusted parameters are $(B_0, \Gamma_0, r, p_e, \gamma_{e,\max}, L_{e,\mathrm{inj}}, L_{p,\mathrm{inj}})$, with $\gamma_{p,\max}$ derived from Eq. (4); for each Model-B zone, they are the shared (B_0, Γ_0) plus $(r, p_e, \gamma_{e,\max}, L_{e,\mathrm{inj}})$. The pure-SSC realization

CPC Accepted

also varies $\gamma_{e,\min}$ in the inner zone. The comparison uses 25 simultaneous *Swift*-XRT and *NuSTAR* spectral points digitized from Fig. 3 of Wierzcholska and Siejkowski [7], with the statistical uncertainties given there. The nominal degrees of freedom are 18 for Model A, 15 for the EC realization, and 14 for the pure-SSC realization. These are manually selected representative solutions, not results of a global parameter search; the reduced χ^2 values are therefore descriptive.

We calculate the synchrotron and inverse-Compton (IC) radiation using the `naima` Python package [17]. In our calculations, synchrotron self-absorption (SSA) is included in both the escaping synchrotron spectrum and the internal synchrotron photon field that provides seed photons for SSC emission, following the radiative-transfer treatment described by Katarzyński et al. [18]. We include $\gamma\gamma$ absorption consistently in all calculations. Specifically, we account for photon-photon absorption within the radiation zones [19], absorption by the external photon fields adopted in the model (including the broad-line region (BLR) and dusty torus (DT) components), and attenuation by the EBL during propagation through intergalactic space [20].

For EC emission and external absorption, we test a phenomenological field normalized by $L_{\rm D} = 10^{42}\,{\rm erg\,s^{-1}}$, at the low-luminosity end of the HBL population [21], with standard BLR and dusty-torus scalings [22]. This is not a detection of a BLR or torus in 1ES 0229+200. In the AGN unification picture, BL Lacs are weak-lined, radiatively inefficient counterparts of more luminous blazars; their external fields should therefore be weak but need not be exactly zero [23]. Even such a weak external photon field can contribute to the emission from a compact region close to the black hole and become more apparent when the dominant synchrotron continuum is exceptionally faint. We therefore retain both an EC solution and a two-zone pure-SSC solution. In the EC solution, the external radiation field is stronger than the magnetic field, with $U'_{\rm ext}/U'_B = 155$ in the inner zone and 36.7 in the outer zone. However, the different appearances of their Compton components are also strongly shaped by the different electron distributions and the corresponding scattering regimes. In particular, inverse-Compton scattering by the higher-energy electrons in the outer zone is increasingly suppressed in the Klein–Nishina regime, and the observed VHE spectrum is further modified by EBL attenuation. In the pure-SSC solution, the external field is set to zero. We adopt $M_{\rm BH} = 1.45\times10^9\,M_\odot$ [24].

A. Model A: One-zone Hybrid Electron–Proton Synchrotron Model

In this scenario, the anomalous 2021 X-ray spectrum is interpreted within a single emission zone located at $r = 0.25$ pc along a jet. This zone contains co-spatial populations of relativistic electrons and protons that radiate via synchrotron processes in the same magnetic field. The jet parameters at the reference distance $r_0 = 0.1$ pc are set to $(\Gamma_0, B_0) = (23, 20\,{\rm G})$, which provides the strong magnetic environment required for proton synchrotron emission in the X-ray band. The corresponding emission-region parameters are shown in Table 1.

Both the electron and proton populations are injected as single power-law distributions, and the resulting steady-state particle distributions are calculated following the method described in Wang et al. [14]. The maximum Lorentz factor of the proton distribution is determined by a gyration-limited acceleration condition,

$$\gamma_{p,\max} = \frac{eBR}{\alpha m_p c^2}, \tag{4}$$

where e is the elementary charge, m_p is the proton rest mass, and α is a factor representing the deviation from the maximum acceleration rate. We adopt $\alpha = 5400$, which corresponds to an upstream shock velocity of $\sim 0.03c$ under the shock acceleration scenario considered by Rieger et al. [25].

The resulting spectral decomposition and the fit to the 2021 low-state X-ray spectrum are shown in Figure 1. The electron synchrotron component dominates the lower-energy X-ray emission and reproduces the underlying soft continuum, while the proton synchrotron component becomes increasingly dominant toward higher energies and produces the spectral hardening above ~ 10 keV. The combination of these two co-spatial synchrotron components produces the concave X-ray shape observed by *NuSTAR*, including the hard X-ray upturn around 25 keV.

Although the calculation included photomeson production, Bethe–Heitler pair production, internal $\gamma\gamma$ absorption, and the subsequent electromagnetic cascade, these components were too weak to be visible in Figure 1. To make this check explicit, Figure 2 shows the full calculation separately. The cascade follows the numerical treatment of Wang et al. [14] and includes the synchrotron, SSC, and EC radiation of secondary pairs. The cascade emission is negligible in the hard-X-ray band and remains below the non-simultaneous MeV–TeV constraints. For the historical *Fermi*-LAT detections shown in Figure 2, the predicted total flux is only 2.6×10^{-4}–9.9×10^{-4} of the measured flux; for the historical VHE points, it is 1.1×10^{-5}–1.6×10^{-4}.

A similar hard X-ray excess has been discussed in other TeV-emitting blazars. For example, multi-wavelength observations of PKS 2155−304 motivated lepto-hadronic modeling in which the observed high-energy emission was partly attributed to hadronic processes, including Bethe–Heitler pair production and the subsequent radiation from secondary particles [27].

CPC Accepted

Table 1. Parameters for Model A and for the EC and pure-SSC realizations of Model B. The jet parameters at the reference distance $r_0 = 0.1$ pc are listed separately. For Model A, $\gamma_{p,\min} = 1$ and $p_p = 2$.

Parameter	Model A	Model B (EC)		Model B (SSC)	
		inner	outer	inner	outer
Jet parameters at $r_0 = 0.1$ pc					
Γ_0	23	35		35	
B_0 (G)	20	0.013		0.0035	
Emission-region parameters					
r (pc)	0.25	0.05	0.10	0.005	0.10
Γ^a	20.2	38.3	35.0	49.3	35.0
δ^a	28.8	31.3	31.7	29.0	31.7
R (cm)^a	2.4×10^{16}	4.8×10^{15}	9.7×10^{15}	4.9×10^{14}	9.7×10^{15}
B (G)^a	8.0	0.026	0.013	0.070	0.0035
Electron distribution					
p_e	1.1	3.0	1.6	2.0	1.6
$\gamma_{e,\min}$	20	20	20	1.1×10^{3}	20
$\gamma_{e,\max}$	4.8×10^{4}	5.0×10^{2}	1.2×10^{6}	2.8×10^{3}	2.4×10^{6}
$L_{e,\mathrm{inj}}$ (erg s^{-1})	1.15×10^{39}	2.73×10^{42}	3.84×10^{40}	6.44×10^{41}	2.66×10^{41}
Proton distribution					
$\gamma_{p,\max}$	1.1×10^{7}	–	–	–	–
$L_{p,\mathrm{inj}}$ (erg s^{-1})	1.70×10^{44}	–	–	–	–
Fit and energetics					
χ^2_r (X-ray only)	1.19	1.41		0.88	
P_e/L_{Edd}	2.57×10^{-6}	2.19×10^{-2}	2.57×10^{-4}	8.57×10^{-3}	1.78×10^{-3}
P_p/L_{Edd}	0.380	–	–	–	–
P_B/L_{Edd}	0.315	4.78×10^{-7}	3.99×10^{-7}	5.75×10^{-8}	2.89×10^{-8}
$P^b_{\mathrm{cold\,p}}/L_{\mathrm{Edd}}$	–	0.804	1.56×10^{-4}	7.10×10^{-3}	8.26×10^{-4}
$P^c_{\mathrm{local}}/L_{\mathrm{Edd}}$	0.695	0.826	4.13×10^{-4}	1.57×10^{-2}	2.61×10^{-3}

[a] Those parameters are not independent free parameters. They are derived from the jet parameters at the reference distance $r_0 = 0.1$ pc using the jet parameterization described before.

[b] Conditional kinetic power of cold protons if one cold proton is assigned to each radiating electron. This matter-content assumption is not part of the radiative fit.

[c] For each zone, $P_i = \pi R^2\Gamma^2 c U'_i$. The local power includes the modeled nonthermal particles, magnetic field, and the conditional cold-proton term where it is listed. Model-B zone powers are reported separately to avoid double-counting the same jet energy flux.

CPC Accepted

However, such models required extremely large proton powers; for some proton distributions, these exceeded the Eddington luminosity by up to three orders of magnitude [27]. In contrast, the proton component required in the present model remains sub-Eddington, as discussed in Section III.

The corresponding energetic requirements of the electron and proton populations are discussed in Section III. This model is constructed specifically to investigate the origin of the anomalous X-ray feature and does not attempt to reproduce the historical HE/VHE emission from 1ES 0229+200 within the same emission zone.

B. Model B: Two-Zone Leptonic Model

We consider two realizations of Model B, each containing two regions embedded in the same jet profile and sharing a common set of (Γ_0, B_0). The EC realization retains $(\Gamma_0, B_0) = (35, 0.013\,\mathrm{G})$ together with the parameters in Table 1. Its outer zone describes the main broadband emission, whereas EC emission from the compact inner zone produces the hard-X-ray component. The inner-zone synchrotron and SSC components are calculated but lie below the plotted range. The required external field is weak and phenomenological.

We also obtain a pure-SSC realization with no BLR or torus photons. It uses $(\Gamma_0, B_0) = (35, 0.0035\,\mathrm{G})$ and the

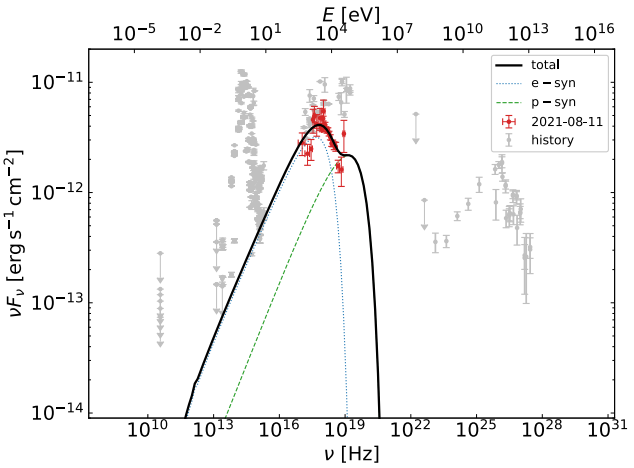

Fig. 1. (color online) Spectral fit of Model A to the anomalous X-ray low state of 1ES 0229+200 observed on 2021 August 11. The black solid line represents the total emission, while the blue dotted and green dashed lines show the electron and proton synchrotron components, respectively. Other unlabeled radiation components have been calculated but are too weak to appear in the plot. The red points represent the simultaneous 2021 *Swift*-XRT and *NuSTAR* spectra used in the fit [7], and the grey points indicate archival multi-wavelength data compiled from the SSDC SED Builder Tool of the Italian Space Agency [26].

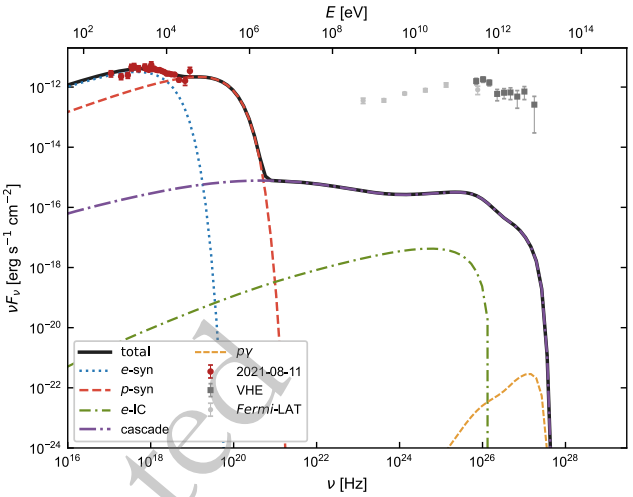

Fig. 2. (color online) Full radiative decomposition of Model A. In addition to primary electron and proton synchrotron radiation and primary electron IC emission, the direct photomeson component and the total secondary-pair cascade are shown. Following Wang et al. [14], the cascade includes photomeson and Bethe–Heitler secondaries and pairs from internal $\gamma\gamma$ absorption, along with their synchrotron, SSC, and EC emission. The pp channel is not included because no cold target gas is assumed.

parameters listed in Table 1. Its X-ray fit statistic is $\chi^2_r = 0.88$. The narrow inner electron distribution shifts its SSC emission into the hard-X-ray band, while the outer-zone SSC emission approximately describes the historical HE/VHE spectrum.

III. DISCUSSION

Three observational limitations define the scope of our interpretation. First, although the data indicate spectral hardening at the highest *NuSTAR* energies, the limited photon statistics above 30 keV render this feature tentative and preclude reliable constraints on its continuation toward higher energies. Second, the source was in an exceptionally low X-ray state, and only gamma-ray upper limits were available during the same period. We therefore use the historical GeV and VHE measurements mainly as reference ceilings: the modeled low-state components should not substantially exceed them, but these measurements are not treated as simultaneous data in the fit. Only in Model B does the outer zone also provide an approximate description of the historical HE/VHE spectrum. Third, the X-ray points used here were digitized from Fig. 3 of Wierzcholska and Siejkowski [7]: they include the simultaneous *Swift*-XRT (0.3–10 keV) and *NuSTAR* (3–40 keV) spectra, which WS25 fitted separately before plotting them together. Our comparison includes both instruments but does not constitute a new fit to their response files. This single observation therefore supports an additional radiative component without determining whether this component is co-spatial or originates in another zone. Similar low-state observations of other EHBLs are needed to test whether this behaviour is common.

The model fits are representative rather than exhaustive. Model A requires $P_p/L_{\rm Edd} = 0.380$ and $P_B/L_{\rm Edd} = 0.315$, so the relativistic-particle and magnetic powers are close to equipartition ($P_p/P_B = 1.21$). Its local magnetic field of 8 G is stronger than in standard SSC fits, but it lies within the range of proton-synchrotron solutions previously obtained for 1ES 0229+200; for example, Cerruti et al. [11] found an acceptable solution with $B = 13$ G and $R = 2.6\times10^{16}$ cm, close to our $B = 8$ G and $R = 2.4\times10^{16}$ cm. The combined proton and magnetic powers amount to $0.695\,L_{\rm Edd}$, indicating that the representative Model A solution is energetically demanding. In comparison, the leptonic realizations require substantially lower nonthermal powers but introduce additional assumptions concerning the presence of multiple electron populations and, in the EC case, a weak external radiation field. These differences illustrate the distinct physical requirements of the hadronic and leptonic interpretations rather than providing a basis for discriminating between them using the current data.

A. An Additional Component in the Anomalous X-ray State

The anomalous X-ray spectrum observed during the

CPC Accepted

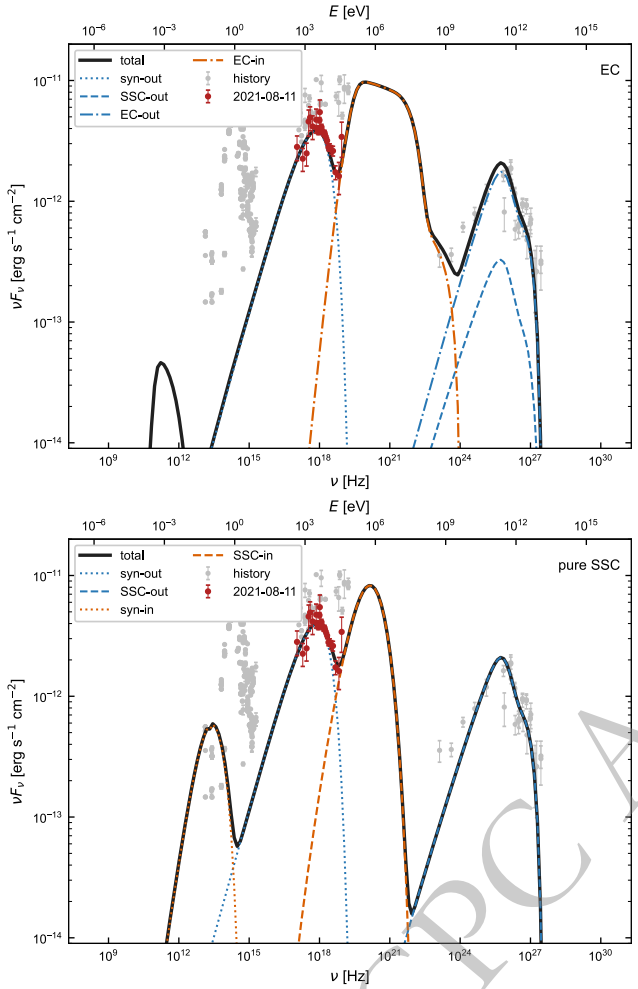

Fig. 3. (color online) The figure is similar to Figure 1 but shows two-zone leptonic solutions. Panel (a) shows the EC solution retained from the original Model B, in which a weak external field provides the inner hard-X-ray component. Panel (b) shows the pure-SSC solution with the external field set to zero. The inner-zone SSC component produces the hard-X-ray upturn, while the outer-zone SSC component approximately describes the historical HE/VHE emission.

extremely low state of 1ES 0229+200 provides a unique opportunity to probe the internal structure of relativistic jets. In a homogeneous one-zone picture, the observed spectral shape is usually interpreted as the direct manifestation of the particle distribution and radiative processes within a single emission region. However, relativistic jets are complex physical systems with spatially varying conditions, and their emission may not always be adequately described by a single homogeneous zone [28]. Direct observational evidence for spatially separated high-energy emission regions has been obtained in resolved extragalactic jets. For example, Clautice et al. [29] showed that the X-ray and radio emission regions in several jet knots do not always coincide spatially, with the X-ray peak located upstream of the radio peak, suggesting the existence of distinct populations of relativistic electrons at different locations along the jet. Although resolved large-scale jets probe physical scales different from those of the compact emitting regions responsible for blazar variability, they demonstrate that spatially distinct particle populations can coexist within relativistic outflows. In this context, blazar emission can be regarded as the superposition of radiation from multiple dissipation regions with different physical conditions; the relative contributions of these regions may vary with time.

This interpretation is closely related to the stochastic dissipation framework developed by Wang et al. [15], in which multiple localized dissipation events embedded in a relativistic jet can naturally produce complex multi-wavelength variability patterns, including orphan flares. In that framework, an unusual spectral state can arise when the contribution of one dissipation region becomes enhanced relative to those of the others. The present observation provides a complementary view of the same physical picture: rather than an additional dissipation event producing an excess during a flare, the extremely low X-ray state may allow a persistent emission component to become visible after the dominant emission regions fade.

The hard X-ray component may be persistent and may become visible only when the soft continuum fades. Such behavior is consistent with a changing mixture of emission components and can naturally arise from spatially distinct dissipation regions, as envisaged in the stochastic dissipation framework, although the present observations do not uniquely require such a spatial separation.

B. Comparison between the Hybrid and Leptonic Interpretations

To investigate the physical origin of the anomalous X-ray spectrum, we constructed two scenarios within the same decelerating-jet framework: a hybrid electron–proton synchrotron model and a purely leptonic two-zone model. Although these scenarios invoke different radiation mechanisms, we compare them under a unified jet parameterization. The representative X-ray fits yield reduced χ^2 values of 1.19 for Model A, 1.41 for the EC realization of Model B, and 0.88 for the pure-SSC realization. These descriptive values do not account for parameter degeneracy, and the inferred powers depend on the assumed particle content.

The main advantage of the hybrid electron–proton synchrotron interpretation is that it can reproduce the anomalous X-ray spectrum within a single emission region. In this scenario, electron synchrotron emission produces the low-energy X-ray continuum, while the proton synchrotron component gradually emerges at higher ener-

CPC Accepted

gies and naturally produces the hard X-ray excess. Thus, the anomalous X-ray spectral curvature can be reproduced by the superposition of electron and proton synchrotron emission from co-spatial particle populations, without introducing an additional electron population to account for the hard X-ray component.

This interpretation requires a relatively strong magnetic field and substantial proton and magnetic power. The two dominant contributions are close to equipartition, and their sum reaches $0.695L_{\rm Edd}$. Such field strengths occur in published proton-synchrotron solutions for this source, so the parameters are demanding but not outside the range already considered for EHBLs. The scope of this interpretation is the X-ray anomaly, not reproduction of the historical HE/VHE emission.

The leptonic interpretation provides a different physical picture. In both realizations, the anomalous X-ray spectrum is reproduced by introducing an additional electron population distinct from that responsible for the underlying broadband emission. In our specific implementations, these populations are assigned to spatially separated regions along the jet: the outer region approximately accounts for the historical broadband synchrotron and IC emission, including the HE/VHE component, while the inner region produces the additional hard X-ray component. The latter is dominated by EC in one realization and by SSC in the other. The spectral data therefore motivate an additional leptonic component, whereas its association with a spatially distinct inner region is a physical realization adopted in our models rather than a unique requirement of the current observations. Different electron populations coexisting within a single emission region may also provide an alternative interpretation.

The two leptonic realizations have complementary limitations. The EC solution permits a broader inner electron distribution and more flexible parameters, but it requires a very weak external radiation field that has not been independently detected. The pure-SSC solution removes that assumption and reproduces the X-ray upturn, but it requires the inner electrons to occupy the narrow interval $1.1\times10^3 \le \gamma_e \le 2.8\times10^3$. Narrow or high-$\gamma_{\rm min}$ electron distributions are a familiar requirement in SSC interpretations of hard-TeV BL Lacs: such distributions have been adopted for 1ES 0229+200 itself [3] and for other hard-TeV sources [30, 31]. In those studies, the narrow distribution hardens the VHE component, whereas here it is required specifically for the additional hard X-ray SSC component. Thus, the analogy concerns the particle-distribution requirement, not an identical emission zone.

The two interpretations should therefore be regarded as different physical realizations of multi-component emission rather than simply as competing single-zone and multi-zone solutions. A structured jet containing spatially distinct dissipation regions provides a natural realization of such a picture, particularly for the leptonic models considered here, but it is not uniquely required by the present spectral data.

C. Future Observational Tests

The current observations are insufficient to uniquely distinguish between the hybrid and leptonic interpretations. Both models provide acceptable descriptions of the available *NuSTAR* spectrum, because the current X-ray coverage samples only the transition region in which the additional hard component begins to emerge. However, the two scenarios predict substantially different spectral behavior beyond the observed energy range.

In the representative Model A solution presented here, the proton-synchrotron component produces the hard-X-ray excess but declines rapidly above this feature. Extending this component to higher energies or increasing its contribution would require different proton-distribution parameters and could increase the required proton power. Given the substantial proton and magnetic powers of this solution, such changes could make the energetic requirements more demanding. Therefore, if future observations reveal a hard-X-ray spectrum that continues to rise significantly beyond the current *NuSTAR* band, the present Model A solution would have difficulty explaining the observed spectrum. Whether alternative parameter choices could alleviate this tension remains to be explored.

The leptonic realizations permit different extensions beyond the observed X-ray band. In the EC realization presented here, the inner EC component forms a broad spectral feature extending from hard X-rays toward the MeV–GeV band, whereas the pure-SSC realization shown here is more confined because of the adopted narrow electron distribution. The latter behavior is parameter-dependent rather than an intrinsic property of SSC emission, since a broader electron distribution could extend the SSC component to substantially higher energies. Future hard-X-ray and MeV observations would therefore constrain not only the radiation mechanism but also the underlying electron distribution.

However, the energy range between the hard X-ray band and the MeV regime remains poorly constrained observationally. The lack of sensitive measurements in this transition region currently prevents clear discrimination between the two scenarios. Future observations covering the MeV band, together with sensitive hard X-ray measurements extending beyond the *NuSTAR* energy range, will therefore provide a critical test of the underlying radiation mechanism.

IV. CONCLUSIONS

We investigated the tentative hard X-ray upturn observed during the exceptionally low X-ray state of 1ES

CPC Accepted

0229+200 on 2021 August 11. Within a common decelerating-jet framework, we tested a one-zone hybrid electron–proton synchrotron model and two realizations of a two-zone leptonic model based on EC and pure SSC.

Model A reproduces the concave X-ray spectrum within one emission region, with electron synchrotron emission dominating the soft band and proton synchrotron emission producing the hard excess. The proton and magnetic powers are close to equipartition and together sum to $0.695L_{\rm Edd}$, and the full photohadronic cascade remains below the level of the historical gamma-ray measurements. In Model B, an outer zone approximately accounts for the historical broadband emission, while a compact inner zone produces the hard X-ray component. The EC realization permits a broader inner electron distribution but requires a weak external photon field, whereas the pure-SSC realization avoids an external photon field at the cost of requiring a narrow inner electron distribution.

Both scenarios therefore lead to the same observational inference: an additional radiative component becomes visible when the dominant soft X-ray continuum fades. The data do not determine whether this component arises from a second particle population in one zone or from a distinct dissipation region. Extending the spectral coverage above the observed upturn and obtaining simultaneous gamma-ray measurements will be essential for selecting between these mechanisms and testing whether the same behaviour occurs in other EHBLs.

CPC Accepted

References

[1] J.-H. Woo, C. M. Urry, R. P. van der Marel, P. Lira, and J. Maza, The Astrophysical Journal **631**, 762 (2005), arXiv: astro-ph/0506316

[2] F. Aharonian, A. G. Akhperjanian, U. Barres de Almeida, A. R. Bazer-Bachi, B. Behera, M. Beilicke, W. Benbow, K. Bernlöhr, C. Boisson, O. Bolz, *et al.*, Astronomy and Astrophysics **475**, L9 (2007), arXiv: 0709.4584

[3] S. Kaufmann, S. J. Wagner, O. Tibolla, and M. Hauser, Astronomy and Astrophysics **534**, A130 (2011), arXiv: 1109.3628

[4] E. Aliu, S. Archambault, T. Arlen, T. Aune, B. Behera, M. Beilicke, W. Benbow, K. Berger, R. Bird, A. Bouvier, *et al.*, The Astrophysical Journal **782**, 13 (2014), arXiv: 1312.6592

[5] F. Tavecchio, G. Ghisellini, G. Ghirlanda, L. Costamante, and A. Franceschini, Mon. Not. R. Astron. Soc. **399**, L59 (2009), arXiv: 0905.0899

[6] J. Hota, R. Khatoon, R. Misra, and A. C. Pradhan, The Astrophysical Journal **976**, 69 (2024), arXiv: 2409.12827

[7] A. Wierzcholska and H. Siejkowski, Astronomy and Astrophysics **703**, A150 (2025), arXiv: 2510.15465

[8] M. Boettcher, arXiv e-prints arXiv: 1006.5048 (2010), 1006.5048.

[9] M. Böttcher, A. Reimer, K. Sweeney, and A. Prakash, The Astrophysical Journal **768**, 54 (2013), arXiv: 1304.0605

[10] M. Cerruti, Galaxies **8**, 72 (2020), arXiv: 2012.13302

[11] M. Cerruti, A. Zech, C. Boisson, and S. Inoue, Mon. Not. R. Astron. Soc. **448**, 910 (2015), arXiv: 1411.5968

[12] F. Tavecchio, A. Costa, and A. Sciaccaluga, Mon. Not. R. Astron. Soc. **517**, L16 (2022), arXiv: 2207.12766

[13] R. Xue, J.-C. He, D. Xiong, and Z.-R. Wang, The Astrophysical Journal **990**, 170 (2025), arXiv: 2508.01986

[14] Z.-R. Wang, R. Xue, D. Xiong, H.-Q. Wang, L.-M. Sun, F.-K. Peng, and J. Mao, The Astrophysical Journal Supplement **271**, 10 (2024), arXiv: 2308.10200

[15] Z.-R. Wang, R.-Y. Liu, M. Petropoulou, F. Oikonomou, R. Xue, and X.-Y. Wang, Physical Review D **105**, 023005 (2022), arXiv: 2112.01739

[16] A. B. Pushkarev, Y. Y. Kovalev, M. L. Lister, and T. Savolainen, Mon. Not. R. Astron. Soc. **468**, 4992 (2017), arXiv: 1705.02888

[17] V. Zabalza, in *34th International Cosmic Ray Conference (ICRC2015)* (2015), vol. 34 of *International Cosmic Ray Conference*, p. 922, 1509.03319.

[18] K. Katarzyński, H. Sol, and A. Kus, Astronomy and Astrophysics **367**, 809 (2001)

[19] R. Xue, Z.-R. Wang, and W.-J. Li, Physical Review D **106**, 103021 (2022), arXiv: 2210.09797

[20] R. C. Gilmore, R. S. Somerville, J. R. Primack, and A. Domínguez, Mon. Not. R. Astron. Soc. **422**, 3189 (2012), arXiv: 1104.0671

[21] Y. Chen, Q. Gu, J. Fan, X. Yu, N. Ding, X. Guo, and D. Xiong, Mon. Not. R. Astron. Soc. **526**, 4079 (2023), arXiv: 2308.15707

[22] M. Hayashida, G. M. Madejski, K. Nalewajko, M. Sikora, A. E. Wehrle, P. Ogle, W. Collmar, S. Larsson, Y. Fukazawa, R. Itoh, *et al.*, The Astrophysical Journal **754**, 114 (2012), arXiv: 1206.0745

[23] G. Ghisellini, F. Tavecchio, L. Foschini, G. Ghirlanda, L. Maraschi, and A. Celotti, Mon. Not. R. Astron. Soc. **402**, 497 (2010), arXiv: 0909.0932

[24] R. M. Wagner, Mon. Not. R. Astron. Soc. **385**, 119 (2008), arXiv: 0711.3025

[25] F. M. Rieger, V. Bosch-Ramon, and P. Duffy, Astrophysics and Space Science **309**, 119 (2007), arXiv: astroph/0610141

[26] G. Stratta, M. Capalbi, P. Giommi, R. Primavera, S. Cutini, and D. Gasparrini, arXiv e-prints arXiv: 1103.0749 (2011), 1103.0749.

[27] H. Abdalla, R. Adam, F. Aharonian, F. Ait Benkhali, E. O. Angüner, M. Arakawa, C. Arcaro, C. Armand, H. Ashkar, M. Backes, *et al.*, Astronomy and Astrophysics **639**, A42 (2020), arXiv: 1912.07273

[28] R. Blandford, D. Meier, and A. Readhead, Annu. Rev. Astron. Astrophys **57**, 467 (2019), arXiv: 1812.06025

[29] D. Clautice, E. S. Perlman, M. Georganopoulos, M. L. Lister, F. Tombesi, M. Cara, H. L. Marshall, B. Hogan, and D. Kazanas, The Astrophysical Journal **826**, 109 (2016), arXiv: 1602.04794

[30] K. Katarzyński, G. Ghisellini, F. Tavecchio, J. Gracia, and L. Maraschi, Mon. Not. R. Astron. Soc. **368**, L52 (2006), arXiv: astro-ph/0603030

[31] L. Costamante, G. Bonnoli, F. Tavecchio, G. Ghisellini, G. Tagliaferri, and D. Khangulyan, Mon. Not. R. Astron. Soc. **477**, 4257 (2018), arXiv: 1711.06282